PNAS RESEARCH ARTICLE | SUSTAINABILITY SCIENCE

Controlled growth of a high selectivity interface for seawater electrolysis

Yang Gao[a], Yurui Xue[a,b,1], Feng He[a], and Yuliang Li[a,c,1]

Edited by Alexis Bell, University of California, Berkeley, Berkeley, CA; received April 21, 2022; accepted July 11, 2022

Overall seawater electrolysis is an important direction for the development of hydrogen energy conversion. The key issues include how to achieve high selectivity, activity, and stability in seawater electrolysis reactions. In this report, the heterostructures of graphdiyne-RhO_x-graphdiyne (GDY/RhO_x/GDY) were constructed by in situ-controlled growth of GDY on RhO_x nanocrystals. A double layer interface of *sp*-hybridized carbon-oxide-Rhodium (*sp*-C∼O-Rh) was formed in this system. The microstructures at the interface are composed of active sites of *sp*-C∼O-Rh. The obvious electron-withdrawing surface enhances the catalytic activity with orders of magnitude, while the GDY outer of the metal oxides guarantees the stability. The electron-donating and withdrawing *sp*-C∼O-Rh structures enhance the catalytic activity, achieving high-performance overall seawater electrolysis with very small cell voltages of 1.42 and 1.52 V at large current densities of 10 and 500 mA cm^{-2} at room temperatures and ambient pressures, respectively. The compositional and structural superiority of the GDY-derived *sp*-C-metal-oxide active center offers great opportunities to engineer tunable redox properties and catalytic performance for seawater electrolysis and beyond. This is a typical successful example of the rational design of catalytic systems.

graphdiyne | high selectivity interface | electron donor and receptor structure | seawater electrolysis | hydrogen energy conversion

Significance

We report a concept catalyst of graphdiyne/rhodium/graphdiyne (GDY/RhO_x/GDY) with bi-layer hetero-interface. The high activity and selectivity of the microstructure formed on the interface results from uncomplete charge transfer between electron donor and acceptor in the system. The high activity and selectivity of catalytic systems due to incomplete charge transfer at the interface is a new concept in the field of catalysis. The catalytic system achieves high-performance overall seawater electrolysis at room temperature and ambient pressure with high current densities of 10 and 500 mA cm^{-2} at 1.42 and 1.52 V, respectively. In the next 5–10 years, such a catalytic system may lead to a big development in the field of catalysis, especially in the direction of electrocatalysis.

Hydrogen is currently the essential feedstock and low-carbon fuel and also the cornerstone of the future energy system (1, 2). The development of hydrogen energy has attracted scientists and engineers around the world. The overall seawater splitting is crucial to large-scale green hydrogen production and the promising way to support the transition to a hydrogen-powered world (3–7). However, efficient seawater splitting was largely limited by the following challenging issues: the high reaction selectivity for oxygen evolution reaction (OER) at the anode and how to avoid the competing chlorine-evolution reaction; sluggish four-electron OER and the hydrogen evolution reaction (HER) processes result in inherently poor reaction kinetics and high overpotentials; low stability and low intrinsic activity of the active sites during electrolysis; and low hydrogen ion (H^+) concentration in seawater that can seriously limit the HER kinetics (8–10). These key issues in seawater electrolysis have attracted wide attention, however, they should also be considered in the overall strategy in this field. Transition metal oxides are well known for their high catalytic activity toward OER from the activity volcano, which correlated the binding energies intermediates on the surface of oxides (11). However, even the most active metal oxide-based OER catalysts are reported to be at least one order magnitude lower than that of natural systems (12). Transition metal oxides HER activities are still far from meeting the demand for scalable hydrogen production from seawater. These serious challenges encourage us to design and synthesize highly selective, active, and robust electrocatalysts to expedite the sluggish overall seawater splitting process, especially at large current densities, to promote the advancements in large-scale hydrogen production.

An ideal catalyst should feature high intrinsic activity with infinite number of active sites at the interface for the adsorption/desorption of reactants or intermediates. One of the efficient strategies is incorporating nanomaterials (e.g., nanocrystals, clusters, etc.) with ideal conductive/active supports to form heterostructures with active interfaces, which can generate more active sites, improve the electron transfer ability, the energy band, the adsorption/desorption energy of reaction intermediates, and thus enhance the electrocatalytic performances (13–15). Rhodium (Rh) possesses excellent hydrogen adsorption-desorption ability with the proper Gibbs free energy. Rh can direct form Rh-oxide nanostructures with Pt-like activity for HER and efficiently oxidize reactant molecules (1, 16, 17). Owing to the tunable chemical/electronic structures, high conductivity, high specific surface area, and excellent stability, carbon materials show great values in catalysis. Combining the advantages of the two materials to produce Rh-oxide-carbon heterojunctions has the potential to greatly improve HER and OER activities and seawater splitting performance.

Author affiliations: [a]CAS Key Laboratory of Organic Solids, Institute of Chemistry, Chinese Academy of Sciences, Beijing 100190, China; [b]Science Center for Material Creation and Energy Conversion, Institute of Frontier and Interdisciplinary Science, School of Chemistry and Chemical Engineering, Shandong University, Jinan 250100, China; and [c]School of Chemical Sciences, University of Chinese Academy of Sciences, Beijing 100049, China

Author contributions: Y.X. and Y.L. designed research; Y.G. performed research; F.H. contributed analytic tools; Y.G. and Y.X. analyzed data; Y.G. wrote the first draft of the paper; Y.X. revised the paper; and Y.L. conceived research and critically revised the paper.

The authors declare no competing interest.

This article is a PNAS Direct Submission.

[1]To whom correspondence may be addressed. Email: yrxue@sdu.edu.cn or ylli@iccas.ac.cn.

This article contains supporting information online at http://www.pnas.org/lookup/suppl/doi:10.1073/pnas.2206946119/-/DCSupplemental.

Published August 29, 2022.

Among all reported carbon materials, porous graphdiyne (GDY) comprised of both *sp*- and sp^2-cohybridized structures has shown many key characteristics compared to traditional carbon materials, in which the large porous and conjugated structures enable efficient diffusion and release of ion/gas. The uneven distribution of surface charges not only enhances the charge transfer ability, but also produces infinite active sites, therefore enhancing the intrinsic activity. The *sp*-C in GDY has been demonstrated to be capable of forming a highly efficient charge transport path. GDY can effectively anchor metal atoms and regulate the nucleation and growth of various nanostructures with different compositions and definite structures of multiple scales and dimensions (18–37).

In this work, we rationally designed a concise route to realize the in situ selective and controllable growth of a two-layer heterojunction based on oxide semiconductor. The graphdiyne/RhO_x/graphdiyne (GDY/RhO_x/GDY) bilayer heterostructure was prepared on RhO_x nanocrystals by perfectly utilizing the advantage that GDY can grow on any substrate. The *sp*-hybrid carbon-oxygen-rhodium (*sp*-C∼O-Rh) double-layer sandwich interface was formed by the heterostructure, which produced a large number of active sites provided by the *sp*-C∼O-Rh interface demonstrating the excellent performance of the catalytic system. Experimental results show that the well-defined *sp*-C∼O-Rh nanostructures catalytic system with donor and receptor structure has strong charge transfer ability, which leads to the rich active sites, excellent electrical conductivity, and ultra-high performance on electrocatalytic activity of the catalytic system. The electrolyzer using GDY/RhO_x/GDY as both the anode and cathode can reach 10 and 500 mA cm^{-2} at low cell voltages of 1.42 and 1.52 V vs. RHE, respectively, which compared favorable to the reported electrocatalysts.

Results

Synthesis and Characterization of GDY/RhO_x/GDY Bilayer Heterostructure. The two-layer heterojunction with *sp*-hybrid carbon-oxygen-rhodium (*sp*-C∼O-Rh) double-layer sandwich interface was constructed through a facile surface-induced growth strategy (Fig. 1). The self-supported three-dimensional (3D) porous GDY electrode was first prepared by growing a film of GDY nanosheets on the smooth surface of 3D carbon fiber cloth (CC). The as-prepared 3D GDY electrode was next immersed in the aqueous solutions of Rh^{3+}, allowing for the anchoring of Rh atoms, which can form the nucleation sites for the controlled growth of Rh oxides nanocrystals on the surface of GDY to form RhO_x/GDY. The GDY/RhO_x/GDY bilayer heterostructure with a new type of *sp*-C∼O-Rh interface was then prepared on RhO_x nanocrystals by perfectly utilizing the advantage of graphdiyne that can grow on any substrate.

Scanning electron microscopy (SEM) (Fig. 2 *A*–*D*) images show the successful growth of a film of ultrathin GDY nanosheets vertically standing over the surface of 3D CC substrates. Remarkably, the GDY nanosheets are interconnected to each other to form an aggregate and produce porous nanostructures. The as-assembled porous aggregate shows a 3D porous hierarchical structure. Such morphology helps to improve the diffusion and release capabilities of ion/gas. A high-resolution transmission electron microscopy (HRTEM) image (*SI Appendix*, Fig. S1) shows that GDY has a lattice spacing of 0.37 nm. After the succesful synthesis of GDY/RhO_x/GDY, the nanosheet array morphology of GDY electrode was well-maintained, and no obvious metal oxides aggregations could be observed on the surface of the electrode (Fig. 2 *E*–*H*). TEM and high-angle annular dark field/bright field scanning TEM (HAADF/BF-STEM) results revealed the well-defined cubic RhO_x nanocrystals grown uniformly and high-density on the surface of GDY (Fig. 2 *I* and *J*), showing the monocrystalline nature of RhO_x on GDY. The lattice spacings for RhO_x (113) planes and GDY are 0.23 and 0.37 nm, respectively (Fig. 2*K*). These results also revealed that the nanosheet morphology of the catalyst and the monocrystalline nature and the cubic shape of RhO_x nanocrystals were well-retained, which also indicates the high stability of the as-synthesized catalyst. Remarkably, the lattice distortion was observed in RhO_x (Fig. 2*L* labeled by the red rectangle), which helps to improve the electrocatalytic performance and stability of the catalysts (38, 39). The histogram analysis showed size distributions of RhO_x (2.29 ± 0.03 nm) (Fig. 2*M*). STEM and elemental mapping images

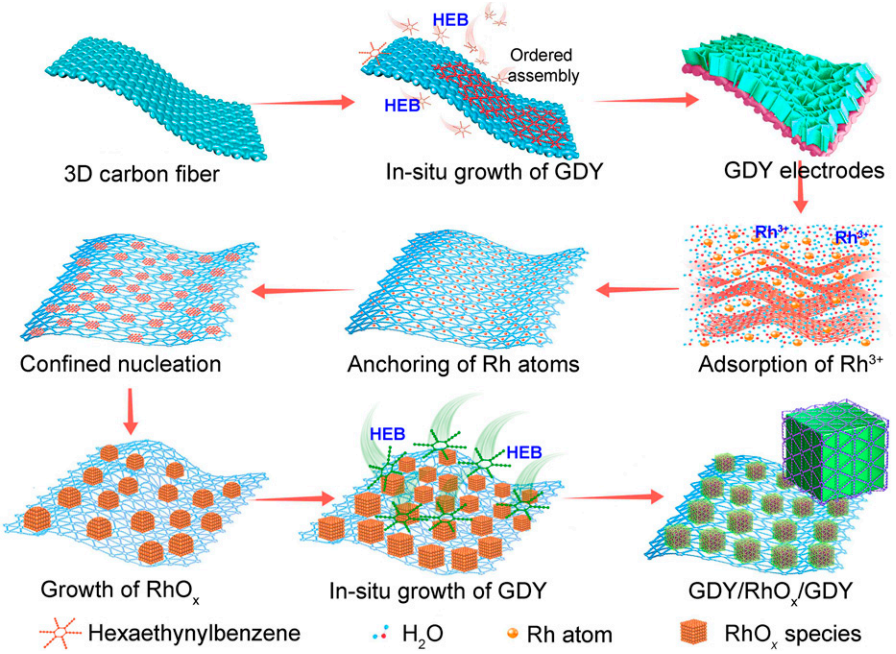

Fig. 1. Synthesis routes to GDY/RhO_x/GDY electrodes through a surface-induced growth strategy.

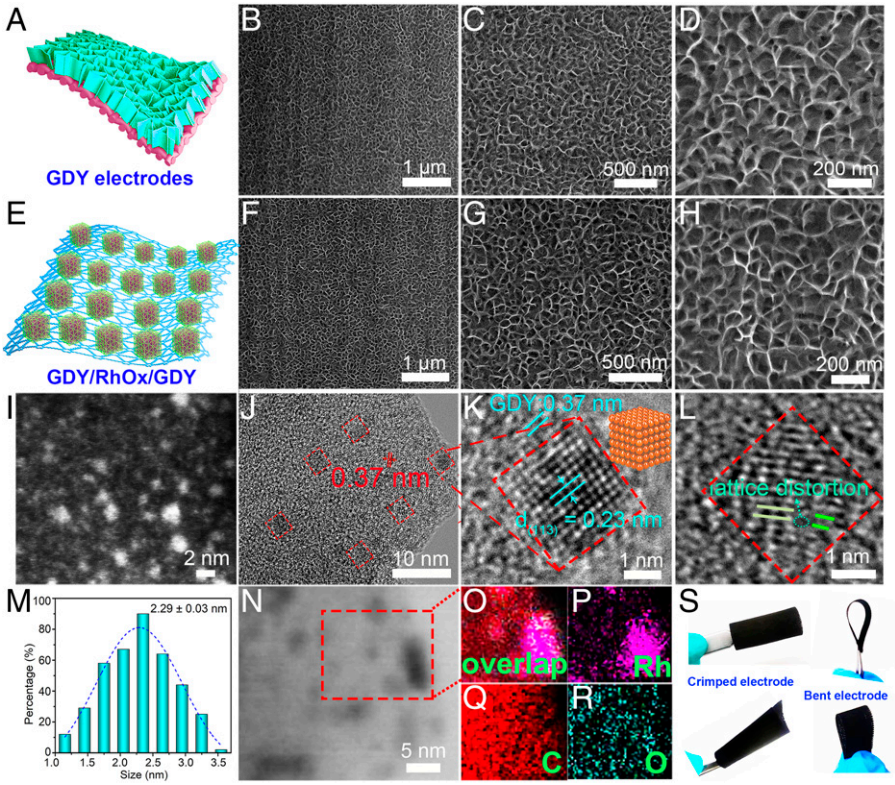

Fig. 2. Morphological characterization. (*A*) Model and (*B–D*) SEM images of GDY electrodes recorded under different magnifications. (*E*) Model and (*F–H*) SEM images of GDY/RhO_x/GDY electrodes recorded under different magnifications. (*I*) High-angle annular dark field scanning TEM (HAADF-STEM) and (*J*) high-resolution TEM images of GDY/RhO_x/GDY. (*K*) HRTEM image of GDY/RhO_x/GDY and (*L*) the lattice distortion of RhO_x. (*M*) The size distribution of RhO_x. (*N*) STEM and (*O–R*) EDS elemental mapping images of GDY/RhO_x/GDY. (*S*) Optical image of GDY/RhO_x/GDY electrodes with different configurations.

confirmed that C, O, and Rh elements uniformly distributed in the nanosheets (Fig. 2 *N–R*). The metal contents in the catalyst were determined by inductive coupled plasma mass spectrometry (ICP-MS) analysis (*SI Appendix*, Table S1). The integrated electrode exhibited outstanding flexibility (Fig. 2*S*), indicating its great promising for practical electrolysis uses.

The structural information of the samples was determined by detailed analysis on the Raman X-ray powder diffraction (XRD), and X-ray photoelectron spectroscopy (XPS) results. Raman spectra of GDY/RhO_x/GDY (*SI Appendix*, Fig. S2) exhibits the typical peaks corresponding to the D (1,371 cm^{-1}) and G (1,593 cm^{-1}) bands and the vibrations of the conjugated diyne links (1,956 and 2,186 cm^{-1}). Compared with pure GDY, these peaks show negative shifts, which indicates the formation of the interactions between GDY and RhO_x resulted from the modification of electronic structures. GDY/RhO_x/GDY has a larger D/G band ratio (I_D/I_G) of 0.8 than (I_D/I_G = 0.62) GDY (*SI Appendix*, Fig. S2). This indicated the more defective structures of GDY/RhO_x/GDY, helping to enhancing catalytic performance. The broad and weak peaks could be well indexed to RhO_x and GDY in the XRD patterns (*SI Appendix*, Fig. S3). The XPS survey spectra (*SI Appendix*, Fig. S4) of GDY/RhO_x/GDY showed the coexistence of Rh, C, and O elements in the catalyst. These results confirmed the successful formation of GDY/RhO_x/GDY.

Detailed XPS analysis of the change in the composition of the sample was further conducted. The XPS survey spectra confirm the coexistence of Rh, C, and O elements in the samples, in accordance with the above energy dispersive X-ray spectroscopy (EDX) results. As shown in Fig. 3*A* and *SI Appendix*, Fig. S5, GDY has four characteristic peaks at 284.5 (sp^2–C), 285.1 (sp–C), 286.6 (C–O), and 288.5 (C=O), respectively. For GDY/RhO_x/GDY, in addition to the peaks of sp^2–C, sp–C, C–O, and C=O, a new peak at 290.0 eV could be ascribed to the π–π^* transition indicating the interactions between GDY and RhO_x (40). Compared with GDY, C 1s XPS peak of GDY/RhO_x/GDY shifted to lower binding energies (BEs) by 0.1 eV, revealing the electron transfer from RhO_x to GDY. The Rh 3d XPS spectrum of GDY/RhO_x/GDY showed two spin-orbit doublets peaks at 309.4/314.1 eV (Rh^{3+} $3d_{5/2}/3d_{3/2}$) and 310.0/314.8 eV (Rh^{4+} $3d_{5/2}/3d_{3/2}$), and satellite peaks at 311.5 and 316.3 eV (Fig. 3*B* and *SI Appendix*, Fig. S6) (41). The high-resolution Rh 3d spectra of RhO_x and GDY/RhO_x/GDY revealed the copresence of $Rh^{3+}$and Rh^{4+}. The ratio of Rh^{4+}/Rh^{3+} (1.25) in GDY/RhO_x/GDY was larger than that of pristine RhO_x (1.19), suggesting that more Rh^{4+} was formed after the formation of the *sp*-C∼O-Rh interfaces. The positive shift by 0.1 eV in BEs of Rh 3d again demonstrated the electron transfer from RhO_x to GDY. These findings confirmed the formation of electron-rich surfaces which benefits the catalytic activity of the catalyst (1, 42, 43). As shown in Fig. 3*C* and *SI Appendix*, Fig. S7, the peak located at 530.7 eV corresponds to the metal-bonded oxygen (metal-O), confirming the formation of Rh-O bonds. The electron energy loss spectroscopy (EELS) mapping of GDY and GDY/RhO_x/GDY (Fig. 3*D* and *SI Appendix*, Fig. S8) shows that only C and Rh signals could be detected, confirming the strong interaction between RhO_x and GDY. As shown in *SI Appendix*, Fig. S9, GDY/RhO_x/GDY has a larger double-layer capacitance (C_{dl}, 4.46 mF cm^{-2}) than that of RhO_x (2.91 mF cm^{-2}), CC (1.30 mF cm^{-2}), and GDY (2.01 mF cm^{-2}). As expected, GDY/RhO_x/GDY possessed the largest electrochemically active surface area (ECSA; 111.5 cm^2) and roughness factor (R_f, 111.5), which demonstrated GDY/RhO_x/GDY had the most active sites after the formation of the unique *sp*-C∼O-Rh interfaces (*SI Appendix*, Table S2).

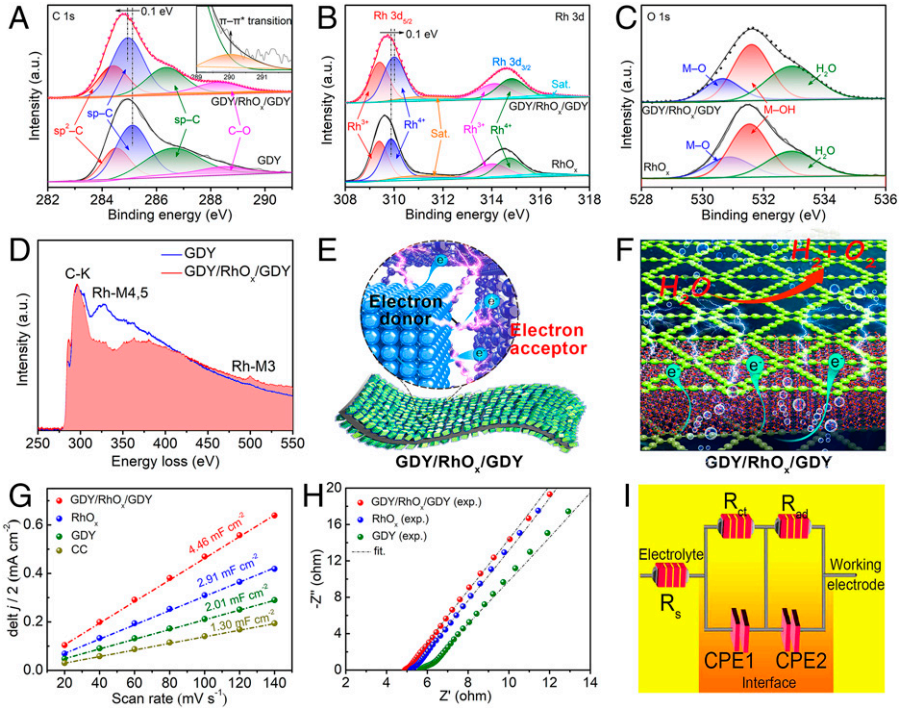

Fig. 3. Structural characterization. The high-resolution (*A*) C 1s, (*B*) Rh 3d, and (*C*) O 1s XPS spectra of the catalysts. (*D*) EELS spectra of carbon and rhodium elements in the GDY and GDY/RhO$_x$/GDY. Schematic representation of (*E* and *F*) the efficient electron transfers from RhO$_x$ to GDY and the electron-rich GDY surface. (*G*) Electrochemical double layer capacitance (C_{dl}) at −0.05 V vs. SCE of the samples. (*H*) Nyquist plots of the catalysts. (*I*) Equivalent model for EIS data fitting.

Electrochemical impedance spectroscopy (EIS) was next performed to reveal the electron/charge transfer ability of the catalysts. Nyquist plots were obtained by EIS measurements (Fig. 3*H* and *SI Appendix*, Table S3). An equivalent circuit model, shown in Fig. 3*I*, (R(QR)(QR)) was used to simulate the data. GDY/RhO$_x$/GDY showed the smallest R_s (resolution resistance, 4.97 Ω) and R_{ct} (charge transfer resistance, 14.22 Ω) than RhO$_x$ (R_s = 5.24 Ω, R_{ct} = 16.21 Ω), GDY (R_s = 5.79 Ω, R_{ct} = 25.57 Ω), and CC (R_s = 5.83 Ω, R_{ct} = 27.52 Ω), indicating the improved charge transfer ability and electrical conductivity of GDY/RhO$_x$/GDY.

Obviously, the formation of the *sp*-C∼O-Rh bonds between GDY and RhO$_x$ was demonstrated to improve the charge transfer ability from RhO$_x$ to GDY, producing the electron-rich surface and more active sites, which might lead to moderate H_2O dissociation and H* adsorption energies, thus greatly enhancing the catalytic performance. As a result, the adsorption/desorption energies for reaction intermediates can be significantly optimized, resulting in a significant enhancement in electrocatalytic performance toward seawater electrolysis.

Electrochemical Seawater Electrocatalysis Performance. Inspired by the superior properties of GDY/RhO$_x$/GDY, the electrocatalytic seawater splitting performances of the catalysts were studied in alkaline-simulated seawater (1.0 M KOH + 0.5 M NaCl aqueous solution, Fig. 4*A*) by a typical three-electrode system. Fig. 4*B* shows the polarization curves for HER with iR-correction. GDY/RhO$_x$/GDY has a much smaller overpotential of 9 mV at 10 mA cm^{-2} and a smaller Tafel slope (42 mV dec^{-1}) than the pure GDY (550 mV@η_{10}, 479 mV dec^{-1}), commercial 20wt% Pt/C (71 mV@η_{10}, 48 mV dec^{-1}), RhO$_x$ (35 mV@η_{10}, 55 mV dec^{-1}), and other reported electrocatalysts (Fig. 4 *B–D* and *SI Appendix*, Tables S4 and S5). These values confirmed the best HER activity of GDY/RhO$_x$/GDY, and the HER might proceed a Heyrovsky dominated Volmer-Heyrovsky mechanism. The specific catalytic activity of the samples was further determined by the exchange current density (j_0), the mass activity, and the turnover frequency (TOF). By extrapolating the Tafel plots, the exchange current density (j_0) of the GDY/RhO$_x$/GDY is measured to be of 1.24 mA cm^{-2}, which is higher than reported electrocatalysts (*SI Appendix*, Table S6) such as W_1Mo_1-NG (0.26 mA cm^{-2}) (44), RhPd-H/C (0.65 mA cm^{-2}) (45), Ru@CQDs480 (0.80 mA cm^{-2}) (46), and Sr_2RuO_4 (0.898 mA cm^{-2}) (47). As shown in *SI Appendix*, Fig. S10, GDY/RhO$_x$/GDY exhibited the higher mass activity than RhO$_x$ and commercial Pt/C at the same overpotentials over a wide range. Moreover, the TOF values of GDY/RhO$_x$/GDY were significantly larger than others (*SI Appendix*, Fig. S11), for example, at an overpotential of 100 mV, the TOF value of GDY/RhO$_x$/GDY was calculated to be 4.36 s^{-1}, higher than RhO$_x$ (1.69 s^{-1}), GDY (0.027 s^{-1}), and recently reported electrocatalysts (*SI Appendix*, Table S7). The catalytic activity of GDY/RhO$_x$/GDY increased significantly with the increasing of experimental temperatures (Fig. 4*E*). As the experimental temperatures increased from 25 °C to 40 °C, 60 °C, and 80 °C, the overpotentials of GDY/RhO$_x$/GDY at 500 mA cm^{-2} decreased from 142 to 131, 118, and 69 mV, respectively, and the Tafel slopes decreased from 42.0 to 36.3, 31.7, and 30.5 mV dec^{-1}, respectively (*SI Appendix*, Fig. S12). The apparent activation energies of the samples were calculated by the Arrhenius equation to compare the intrinsically catalytic activity of the catalysts. As expected, GDY/RhO$_x$/GDY has activation energies of 16.83 kJ mol^{-1} (45 mV), 18.31 kJ mol^{-1} (50 mV), and 20.39 kJ mol^{-1} (55 mV), which are smaller than reported catalysts, indicating the excellent catalytic activity of GDY/RhO$_x$/GDY (Fig. 4*F*). According to above results, we can postulate that the enhanced catalytic activity can be ascribed to *sp*-C∼O-Rh active centers formed at the interface between GDY and RhO$_x$.

In addition to initial catalyst activity, the long-term stability is another important aspect for the practical applications. As shown in Fig. 4*G*, there are no decreases in the current densities even

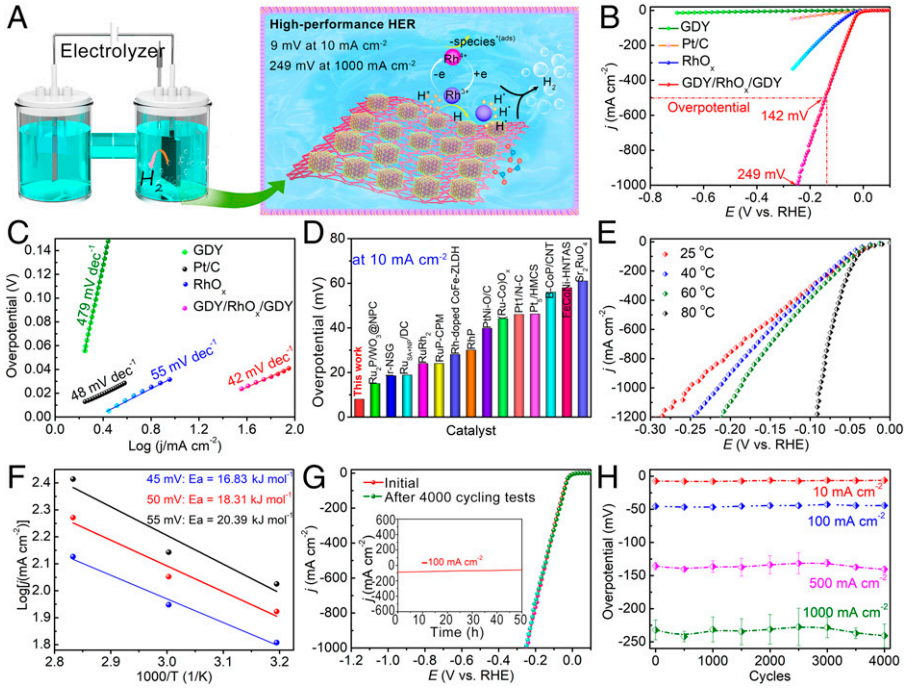

Fig. 4. Electrochemical seawater reduction performance. (*A*) Schematic illustration of GDY/RhO_x/GDY working as an electrocatalyst for efficient seawater reduction. (*B*) HER polarization curves and (*C*) corresponding Tafel plots of as-synthesized catalysts. (*D*) Comparison of the HER activity with reported catalysts. (*E*) HER LSV curves recorded at various temperatures. (*F*) Arrhenius plots for the HER performed over GDY/RhO_x/GDY at various potentials. (*G*) Durability stability tests of GDY/RhO_x/GDY over 4,000 cycles (*Inset*: time-current density curve of GDY/RhO_x/GDY at −100 mA cm^{-2}). (*H*) The overpotentials of GDY/RhO_x/GDY over 4,000 cycles recorded at 10, 100, 500, and 1,000 mA cm^{-2}. Error bars indicate the SD of the current density.

over 4,000-cycle continuous cycling voltammetry (CV) tests. The time-current density curve of GDY/RhO_x/GDY recorded at −100 mA cm^{-2} exhibits negligible losses in current density (inset in Fig. 4*G*). Besides, the overpotentials at 10, 100, 500, and 1,000 mA cm^{-2} for three independent experiments were all well retained after such long-term stability tests (Fig. 4*H*). SEM (*SI Appendix*, Fig. S13) and TEM (*SI Appendix*, Fig. S14) images confirmed the excellent stability of the catalyst without any aggregation. The elements C, O, and Rh were homogeneously distributed within the whole GDY structure, as evidenced by a TEM-EDX test (*SI Appendix*, Fig. S15). These results all confirmed the outstanding stability of GDY/RhO_x/GDY for hydrogen production from seawater.

The OER catalytic performances of GDY/RhO_x/GDY were next studied in alkaline simulated seawater electrolytes. As shown in Fig. 5*A*, GDY/RhO_x/GDY exhibits the best OER activity with the smallest overpotentials of 193 and 261 mV at 10 and 100 mA cm^{-2} than RuO_2, RhO_x, GDY, and previously reported electrocatalysts (*SI Appendix*, Table S8). GDY/RhO_x/GDY shows a smaller Tafel slope of 68 mV dec^{-1} (Fig. 5*B*) than RuO_2 (79 mV dec^{-1}) and most of the reported precious and nonprecious electrocatalysts (*SI Appendix*, Table S8), which reveals the faster reaction kinetics of GDY/RhO_x/GDY. To evaluate the stability characteristics of GDY/RhO_x/GDY, continuous potential cycling and chronoamperometry tests were carried out, as shown in Fig. 5*C*. The continuous potential cycling tests show almost no decrease in the OER activity even after 10,000-cycle tests. The chronoamperometry test results show a slow loss in activity at large current densities around 500 mA cm^{-2} (Fig. 5*D*). SEM (*SI Appendix*, Fig. S16 *A* and *B*), TEM (*SI Appendix*, Fig. S16 *C* and *D*) and Raman (*SI Appendix*, Fig. S17) results confirmed the high stability of the catalysts during the electrolysis process. Inspired by such excellent HER and OER performances, we assembled a seawater electrolyzer using GDY/RhO_x/GDY as both anodic and cathodic electrodes (Fig. 5 *E*–*G* and Movie S1). GDY/RhO_x/GDY||GDY/RhO_x/GDY showed the best overall seawater splitting activity with the smallest cell voltages of 1.42, 1.49, and 1.52 V at 10, 100, and 500 mA cm^{-2}, respectively, which are better than RuO_2||Pt/C (1.56 and 1.71 V at 10 and 100 mA cm^{-2}, respectively), RhO_x||RhO_x (1.62 V at 10 mA cm^{-2}), GDY||GDY (1.81 V at 10 mA cm^{-2}), and other reported state-of-the-art electrodes (*SI Appendix*, Table S9), including NiMoN nanorods(+)//NiMoN nanorods(−) (1.56 V at 100 mA cm^{-2}) (48) and Co-Fe_2P(+)//Co-Fe_2P(−) (1.69 V at 100 mA cm^{-2}) (49), respectively. Moreover, the catalytic activity of the GDY/RhO_x/GDY||GDY/RhO_x/GDY can be maintained over 13,000 continuous cycling tests (Fig. 5*H*) and can deliver 100 and 500 mA cm^{-2} more than 53 h at the cell voltage of 1.49 V and 1.52 V (Fig. 5*I*). These results demonstrate the excellent long-term stability of GDY/RhO_x/GDY for overall seawater splitting. From the above experimental results, we can see that the formation of the interfaces composed of active sites of *sp*-C∼O-Rh can effectively enhance the catalytic activity. As shown in *SI Appendix*, Figs. S18 and S19, the as-synthesized GDY/RhO_x/GDY in pure alkaline solution shows similar catalytic activities to that obtained in the alkaline-simulated seawater conditions. The catalytic activity of GDY/RhO_x/GDY could be influenced by the mass loading of RhO_x. The catalytic activities for HER, OER, and overall seawater splitting increased initially with the increasing of the mass loading of RhO_x, then decreased with further increase in the mass loading (*SI Appendix*, Figs. S20 and S21). This is due to the aggregation of the RhO_x species (*SI Appendix*, Fig. S22). Furthermore, the catalytic activities of the catalysts supported on the glassy carbon electrode (GCE) (*SI Appendix*, Figs. S23 and S24) and other carbon substrates (*SI Appendix*, Figs. S25 and S26), such as graphene oxide (GO) and multiwall carbon nanotubes (MWCNT), were all tested. As expected, GDY/RhO_x/GDY exhibited the best catalytic activity than those supported by GCE and other carbon substrates.

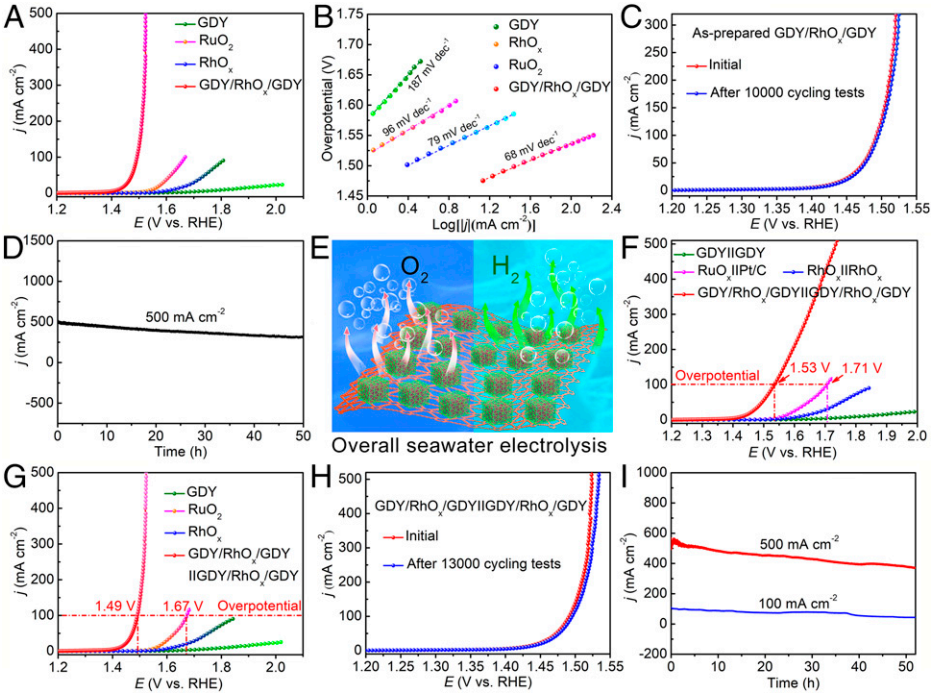

Fig. 5. Electrochemical seawater oxidation and overall seawater splitting performances. (*A*) OER LSV curves and (*B*) corresponding Tafel plots of as-synthesized samples. (*C*) Polarization curves of GDY/RhO$_x$/GDY recorded before and after 10,000 continuous cycles of the OER. (*D*) Chronoamperometry test of GDY/RhO$_x$/GDY. (*E*) Schematic representation of the overall seawater splitting process. LSV curves of the catalysts for overall seawater splitting recorded (*F*) before and (*G*) after the iR-correction. (*H*) LSV curves of GDY/RhO$_x$/GDY recorded before and after 13,000 continuous cycles for overall seawater splitting. (*I*) Chronoamperometry test of GDY/RhO$_x$/GDY for overall seawater splitting at 500 and 100 mA cm^{-2}.

For further insights into the origin of the catalytic activity, XPS measurements on the samples during the seawater splitting process were carried out to determine the variation of the surface composition of GDY/RhO$_x$/GDY along with the changes of the catalytic activity (*SI Appendix*, Fig. S27). The *sp*–C peaks for GDY in the electrocatalyst shift to higher binding energies (*SI Appendix*, Fig. S28), while the Rh 3d XPS spectra shifted to lower binding energies from 309.40 eV (freshly-synthesized catalyst) to 309.36 eV (after 1,000 cycles) and 309.2 eV (after 4,000 cycles) (Fig. 6 *A*–*C*). It was observed that the valence states of Rh species decreased as the HER electrocatalysis proceeded. Compared with the freshly synthesized GDY/RhO$_x$/GDY, the percentage of Rh^{3+} was gradually increased while the Rh^{4+} content decreased (Fig. 6*D*), which demonstrates that the Rh^{4+} might play an important role in enhancing the catalytic activity. In the O 1s XPS spectra, we observed a significant increase in the 531.40–531.60 eV peak (hydroxide species) intensity during the HER process (Fig. 6 *E* and *F*), which suggests the formation of more surface hydroxides (RhOOH) on the surface of the catalysts. These results reveal that the mixed valent of Rh^{3+}/Rh^{4+} and the

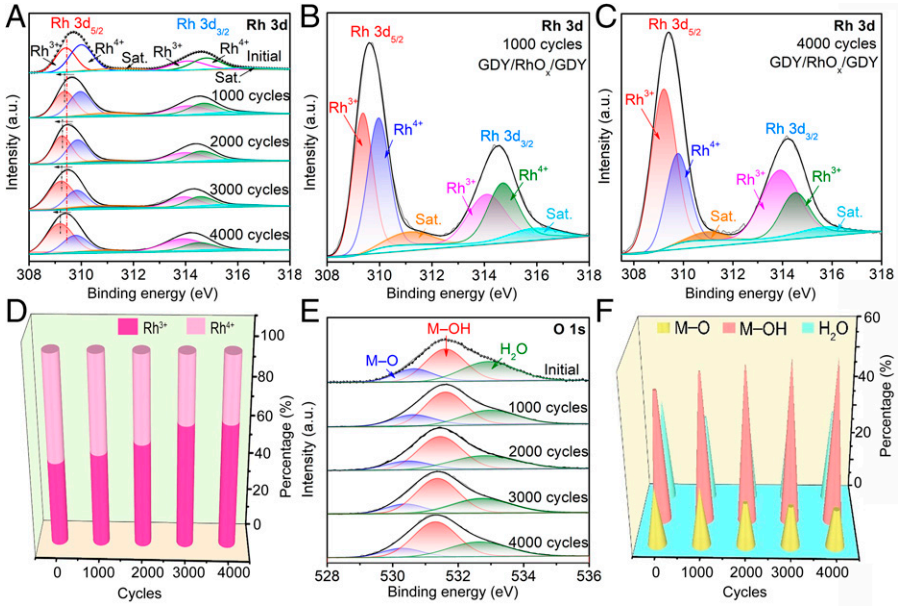

Fig. 6. (*A*) Rh 3d XPS spectra of GDY/RhO$_x$/GDY recorded before and after cycling tests of 1,000, 2,000, 3,000, and 4,000 cycles. High-resolution of Rh 3d XPS spectra of GDY/RhO$_x$/GDY recorded after (*B*) 1,000 and (*C*) 4,000 cycles. (*D*) Percentage of Rh^{3+} and Rh^{4+} in GDY/RhO$_x$/GDY after cycling tests. (*E*) Rh 3d XPS spectra of GDY/RhO$_x$/GDY recorded before and after cycling tests of 1,000, 2,000, 3,000, and 4,000 cycles. (*F*) Percentage of M−O, −OH, and H_2O species.

Rh hydroxides on the surface the catalysts all play an important role in improving the electrocatalyst activity.

Discussion

This work reports the in situ-controlled growth of two-layer heterostructures of GDY/RhO_x/GDY by utilizing the advantages of GDY that can be grown on any substrate, improved charge transport ability, large number of active sites, highly intrinsic activity, and optimal adsorption/desorption ability. A sp-C∼O-Rh catalytic system with donor and receptor structure obviously enhances the catalytic activity with orders of magnitude, while the GDY outer of the metal oxides guarantees the stability. As expected, we have achieved the high-performance overall seawater electrolysis with very small cell voltages of 1.42 and 1.52 V at 10 and 500 mA cm^{-2}, respectively, for overall alkaline seawater splitting at room temperatures and ambient pressures. This work represents a step forward toward designing active centers with determined structures to electrocatalysis.

Materials and Methods

Additional details regarding the *Materials and Methods* may be found in the *SI Appendix*.

Synthesis of RhO_x/GDY. RhO_x/GDY was prepared through a hydrothermal reaction. Typically, $RhCl_3 \times xH_2O$ (39%, 0.17 mg mL^{-1}) aqueous solution and the GDY sample were added into a 30 mL Teflon-lined stainless-steel autoclave. After being kept at 150 °C for 7 h, the RhO_x/GDY was obtained.

The RhO_x grown on the surface of CC, GO, and MCWNT were obtained by replacing GDY with pure CC, GO, and MCWNT substrates, respectively.

Synthesis of GDY/RhO_x/GDY. GDY/RhO_x/GDY was synthesized by in situ growth of the GDY on RhO_x/GDY at 50 °C for 12 h in a 0.4-mg mL^{-1} HEB pyridine solution under Ar. The samples were washed by acetone and DMF several times to remove residual impurities and dried at room temperature in vacuum. The GDY/RhO_x/GDY was finally obtained and washed with deionized water several times.

Characterization. SEM (Hitachi S-4800), TEM (JEM-2100F), and high-resolution TEM were used to determine the morphologies. The elemental mapping images were obtained by EDX. The high-angle annular dark field/bright field scanning TEM (HAADF/BF-STEM) was measured on a JEM-ARM200F (JEOL). Raman spectra were obtained by the Renishaw-2000 Raman spectrometer (473 nm excitation laser). XPS (Thermo Scientific ESCALab 250Xi instrument with monochromatic Al Kα), XRD (Rigaku D/max-2500) equipped with Cu Kα radiation ($\lambda = 1.54178$ Å) were used to determine the structure of samples. ELLS images were collected using Titan Themis300. ICP-MS (Thermo Fisher) was used to determine the mass loading. Rh mass loadings in GDY/RhO_x/GDY and RhO_x were 1.36 and 1.568 μg_{Rh} cm^{-2}, respectively.

Data Availability. All study data are included in the article and/or *SI Appendix*.

ACKNOWLEDGMENTS. We acknowledge the support from the National Key Research and Development Project of China (2018YFA0703501), the National Nature Science Foundation of China (21790050, 21790051, and 22021002), the Key Program of the Chinese Academy of Sciences (XDPB13), and the Postdoctoral Science Foundation of China (2019M660806).

1. Z. W. Seh *et al.*, Combining theory and experiment in electrocatalysis: Insights into materials design. *Science* **355**, eaad4998 (2017).
2. S. J. Davis *et al.*, Net-zero emissions energy systems. *Science* **360**, eaas9793 (2018).
3. R. Subbaraman *et al.*, Enhancing hydrogen evolution activity in water splitting by tailoring Li^+-$Ni(OH)_2$-Pt interfaces. *Science* **334**, 1256 (2011).
4. S. Chu, Y. Cui, N. Liu, The path towards sustainable energy. *Nat. Mater.* **16**, 16–22 (2016).
5. C. Niether *et al.*, Improved water electrolysis using magnetic heating of FeC–Ni core–shell nanoparticles. *Nat. Energy* **3**, 476–483 (2018).
6. S. Z. Oener, M. J. Foster, S. W. Boettcher, Accelerating water dissociation in bipolar membranes and for electrocatalysis. *Science* **369**, 1099–1103 (2020).
7. W. Zang *et al.*, Efficient hydrogen evolution of oxidized Ni-N_3 defective sites for alkaline dreshwater and seawater electrolysis. *Adv. Mater.* **33**, e2003846 (2021).
8. L. Wu *et al.*, Heterogeneous bimetallic phosphide Ni_2P-Fe_2P as an efficient bifunctional catalyst for water/seawater splitting. *Adv. Funct. Mater.* **31**, 2006484 (2021).
9. H. Jin *et al.*, Stable and highly efficient hydrogen evolution from seawater enabled by an unsaturated nickel surface nitride. *Adv. Mater.* **33**, e2007508 (2021).
10. W. Xu *et al.*, Electronic structure modulation of nanoporous cobalt phosphide by carbon doping for alkaline hydrogen evolution reaction. *Adv. Funct. Mater.* **31**, 2107333 (2021).
11. I. C. Man *et al.*, Universality in oxygen evolution electrocatalysis on oxide surfaces. *ChemCatChem* **3**, 1159–1165 (2011).
12. K. N. Ferreira, T. M. Iverson, K. Maghlaoui, J. Barber, S. Iwata, Architecture of the photosynthetic oxygen-evolving center. *Science* **303**, 1831–1838 (2004).
13. N. Wang *et al.*, In situ confinement of ultrasmall Pd clusters within nanosized silicalite-1 zeolite for highly efficient catalysis of hydrogen generation. *J. Am. Chem. Soc.* **138**, 7484–7487 (2016).
14. H. Shen, Y. Li, Y. Li, Self-assembly and tunable optical properties of intramolecular charge transfer molecules. *Aggregate* **1**, 57–68 (2020).
15. N. Wang *et al.*, Impregnating subnanometer metallic nanocatalysts into self-pillared zeolite nanosheets. *J. Am. Chem. Soc.* **143**, 6905–6914 (2021).
16. H. Liu *et al.*, Efficient electrochemical nitrate reduction to ammonia with copper supported rhodium cluster and single-atom catalysts. *Angew. Chem. Int. Ed. Engl.* **61**, e202202556 (2022).
17. X.-N. Li, H.-M. Zhang, Z. Yuan, S.-G. He, A nine-atom rhodium-aluminum oxide cluster oxidizes five carbon monoxide molecules. *Nat. Commun.* **7**, 11404 (2016).
18. G. Li *et al.*, Architecture of graphdiyne nanoscale films. *Chem. Commun. (Camb.)* **46**, 3256–3258 (2010).
19. Y. Fang, Y. Liu, L. Qi, Y. Xue, Y. Li, 2D graphdiyne: An emerging carbon material. *Chem. Soc. Rev.* **51**, 2681–2709 (2022).
20. C. Huang *et al.*, Progress in research into 2D graphdiyne-based materials. *Chem. Rev.* **118**, 7744–7803 (2018).
21. Y. Du, W. Zhou, J. Gao, X. Pan, Y. Li, Fundament and application of graphdiyne in electrochemical energy. *Acc. Chem. Res.* **53**, 459–469 (2020).
22. Y. Xue *et al.*, Anchoring zero valence single atoms of nickel and iron on graphdiyne for hydrogen evolution. *Nat. Commun.* **9**, 1460 (2018).
23. L. Hui *et al.*, Highly efficient and selective generation of ammonia and hydrogen on a graphdiyne-based catalyst. *J. Am. Chem. Soc.* **141**, 10677–10683 (2019).
24. L. Hui *et al.*, Highly dispersed platinum chlorine atoms anchored on gold quantum dots for a highly efficient electrocatalyst. *J. Am. Chem. Soc.* **144**, 1921–1928 (2022).
25. C. Xing *et al.*, Fluorographdiyne: A metal-free catalyst for applications in water reduction and oxidation. *Angew. Chem. Int. Ed. Engl.* **58**, 13897–13903 (2019).
26. J.-C. Liu, H. Xiao, J. Li, Constructing high-loading single-atom/cluster catalysts via an electrochemical potential window strategy. *J. Am. Chem. Soc.* **142**, 3375–3383 (2020).
27. J. Li *et al.*, Graphdiyne: A metal-free material as hole transfer layer to fabricate quantum dot-sensitized photocathodes for hydrogen production. *J. Am. Chem. Soc.* **138**, 3954–3957 (2016).
28. Y. Fang, Y. Xue, L. Hui, H. Yu, Y. Li, Graphdiyne@Janus magnetite for photocatalytic nitrogen fixation. *Angew. Chem. Int. Ed. Engl.* **60**, 3170–3174 (2021).
29. C. Pan *et al.*, Neighboring sp-hybridized carbon participated molecular oxygen activation on the interface of sub-nanocluster CuO/graphdiyne. *J. Am. Chem. Soc.* **144**, 4942–4951 (2022).
30. Z. Zheng, L. Qi, Y. Xue, Y. Li, Highly selective and durable of monodispersed metal atoms in ammonia production. *Nano Today* **43**, 101431 (2022).
31. Q. Lv *et al.*, Selectively nitrogen-doped carbon materials as superior metal-free catalysts for oxygen reduction. *Nat. Commun.* **9**, 3376 (2018).
32. X. Gao, H. Liu, D. Wang, J. Zhang, Graphdiyne: Synthesis, properties, and applications. *Chem. Soc. Rev.* **48**, 908–936 (2019).
33. Y. Zhao *et al.*, Few-layer graphdiyne doped with sp-hybridized nitrogen atoms at acetylenic sites for oxygen reduction electrocatalysis. *Nat. Chem.* **10**, 924–931 (2018).
34. Y. Zhao *et al.*, Stereodefined codoping of sp-N and S atoms in few-layer graphdiyne for oxygen evolution reaction. *J. Am. Chem. Soc.* **141**, 7240–7244 (2019).
35. Y. Xue, Y. Li, J. Zhang, Z. Liu, Y. Zhao, 2D graphdiyne materials: Challenges and opportunities in energy field. *Sci. China Chem.* **61**, 765–786 (2018).
36. X.-P. Yin *et al.*, Engineering the coordination environment of single-atom platinum anchored on graphdiyne for optimizing electrocatalytic hydrogen evolution. *Angew. Chem. Int. Ed. Engl.* **57**, 9382–9386 (2018).
37. S. Zhang *et al.*, Graphdiyne: Bridging SnO_2 and perovskite in planar solar cells. *Angew. Chem. Int. Ed. Engl.* **59**, 11573–11582 (2020).
38. R. Jin, G. Li, S. Sharma, Y. Li, X. Du, Toward active-site tailoring in heterogeneous catalysis by atomically precise metal nanoclusters with crystallographic structures. *Chem. Rev.* **121**, 567–648 (2021).
39. J. Liang *et al.*, Atomic arrangement engineering of metallic nanocrystals for energy-conversion electrocatalysis. *Joule* **3**, 956–991 (2019).
40. S. Yuan *et al.*, Tunable metal hydroxide-organic frameworks for catalysing oxygen evolution. *Nat. Mater.* **21**, 673–680 (2022).
41. Z. Li *et al.*, Stable rhodium (IV) oxide for alkaline hydrogen evolution reaction. *Adv. Mater.* **32**, e1908521 (2020).
42. F. Wang, W. Ueda, J. Xu, Detection and measurement of surface electron transfer on reduced molybdenum oxides ($MoO_{(x)}$) and catalytic activities of Au/$MoO_{(x)}$. *Angew. Chem. Int. Ed. Engl.* **51**, 3883–3887 (2012).
43. G. W. Sievers *et al.*, Self-supported Pt-CoO networks combining high specific activity with high surface area for oxygen reduction. *Nat. Mater.* **20**, 208–213 (2021).
44. Y. Yang *et al.*, O-coordinated W-Mo dual-atom catalyst for pH-universal electrocatalytic hydrogen evolution. *Sci. Adv.* **6**, eaba6586 (2020).
45. J. Fan *et al.*, Hydrogen stabilized RhPdH 2D bimetallene nanosheets for efficient alkaline hydrogen evolution. *J. Am. Chem. Soc.* **142**, 3645–3651 (2020).
46. W. Li *et al.*, Carbon-quantum-dots-loaded ruthenium nanoparticles as an efficient electrocatalyst for hydrogen production in alkaline media. *Adv. Mater.* **30**, e1800676 (2018).
47. Y. Zhu *et al.*, Unusual synergistic effect in layered Ruddlesden-Popper oxide enables ultrafast hydrogen evolution. *Nat. Commun.* **10**, 149 (2019).
48. L. Yu *et al.*, Non-noble metal-nitride based electrocatalysts for high-performance alkaline seawater electrolysis. *Nat. Commun.* **10**, 5106 (2019).
49. S. Wang *et al.*, Synthesis of 3D heterostructure Co-doped Fe_2P electrocatalyst for overall seawater electrolysis. *Appl. Catal. B* **297**, 120386 (2021).